



HAL
open science

Diagnosing concurrent drivers of weather extremes: application to hot and cold days in North America

Davide Faranda, Gabriele Messori, Pascal Yiou

► **To cite this version:**

Davide Faranda, Gabriele Messori, Pascal Yiou. Diagnosing concurrent drivers of weather extremes: application to hot and cold days in North America. 2019. hal-02095205v1

HAL Id: hal-02095205

<https://hal.science/hal-02095205v1>

Preprint submitted on 10 Apr 2019 (v1), last revised 7 Nov 2019 (v2)

HAL is a multi-disciplinary open access archive for the deposit and dissemination of scientific research documents, whether they are published or not. The documents may come from teaching and research institutions in France or abroad, or from public or private research centers.

L'archive ouverte pluridisciplinaire **HAL**, est destinée au dépôt et à la diffusion de documents scientifiques de niveau recherche, publiés ou non, émanant des établissements d'enseignement et de recherche français ou étrangers, des laboratoires publics ou privés.

1 **Diagnosing concurrent drivers of weather extremes:**
2 **application to hot and cold days in North America**

3 **Davide Faranda · Gabriele Messori ·**
4 **Pascal Yiou**

5
6 Received: date / Accepted: date

7 **Abstract** A fundamental challenge in climate science is decomposing the con-
8 current drivers of weather extremes in observations. Achieving this would pro-
9 vide insights into the drivers of individual extreme events as well as into pos-
10 sible future changes in extreme event frequencies under greenhouse forcing.
11 In the present work, we exploit recent results from dynamical systems the-
12 ory to study the co-variation and recurrence statistics of different atmospheric
13 fields. Specifically, we present a methodology to quantify the recurrences of
14 bivariate fields, the repeated co-occurrences of distinct univariate fields, and
15 the dependence between two fields. The dependence is defined by a coupling
16 parameter, which varies according to the chosen fields, season, and domain
17 and can be understood in terms of the underlying physics of the atmosphere.
18 For suitably chosen fields, this approach enables to decompose the different
19 drivers of weather extremes. Here, we compute the above metrics for near-
20 surface temperature and sea level pressure, and use them to study hot or cold
21 days over North America. We first identify states where temperature extremes
22 are strongly and weakly coupled to the large-scale atmospheric circulation,
23 and then elucidate the interplay between coupling and the occurrence of tem-
24 perature extremes.

D. Faranda

Laboratoire des Sciences du Climat et de l'Environnement LSCE-IPSL, CEA Saclay l'Orme
des Merisiers, UMR 8212 CEA-CNRS-UVSQ, Université Paris-Saclay, 91191 Gif-sur-Yvette,
France & London Mathematical Laboratory, 8 Margravine Gardens, London, W68RH, UK.
E-mail: davide.faranda@lsce.ipsl.fr

G. Messori

Department of Earth Sciences, Uppsala University, Uppsala, Sweden & Department of Me-
teorology and Bolin Centre for Climate Research, Stockholm University, Stockholm, Sweden

P. Yiou

Laboratoire des Sciences du Climat et de l'Environnement LSCE-IPSL, CEA Saclay l'Orme
des Merisiers, UMR 8212 CEA-CNRS-UVSQ, Université Paris-Saclay, 91191 Gif-sur-Yvette,
France

25 **Keywords** Weather extremes · Analogues · Climate Dynamics · Dynamical
26 Systems Theory

27 1 Introduction

28 Weather extremes are complex events, driven by a variety of physical pro-
29 cesses. Disentangling these processes is a fundamental challenge in climate
30 science and is essential in order to reconstruct the process-chain leading to
31 individual or co-occurring extremes (Davies, 2015; Harnik et al, 2016). Early
32 statistical studies of weather extremes have adopted a univariate framework,
33 projecting extreme events onto peak-over-threshold (Pickands III, 1975) or
34 block-maxima (Gnedenko, 1943) of single observables (e.g. storm surges, wind
35 speeds or temperatures (Galambos et al, 1994)). Multivariate approaches have
36 been introduced to take into account combinations of variables that achieve
37 simultaneously large or small values (e.g. wind-speed and storm surge). Re-
38 cently, the awareness has grown that individual variables may not be extreme
39 themselves, but their joint occurrence may yield an extremal behavior (see e.g.
40 Bevacqua et al (2017)).

41 In order to understand the root drivers of large-scale weather extremes,
42 one must therefore follow all the relevant variables in space and time over
43 extended regions. For example, heatwaves or cold spells reflect the interac-
44 tion between persistent circulation regimes and temperature patterns, that
45 exacerbate each other. In some cases additional confounding factors, such as
46 soil-moisture levels, further complicate the picture (Zscheischler and Senevi-
47 ratne, 2017). Studying these interplays a priori necessitates a large number of
48 numerical experiments with multi-parameter models.

49 In this paper, we aim to combine a multivariate view of extremes with
50 analytical and computational efficiency, by constraining the analyses with the
51 generic behavior of chaotic systems. We propose a new methodology, based on
52 the adaptation and extension of recent mathematical results from dynamical
53 systems theory, and apply it to the study of temperature extremes (hot or cold
54 days) over North America. For the latter part, we build upon the numerous
55 studies that have tried to connect the dynamical properties of the atmosphere
56 to the occurrence of temperature extremes in the region (Grotjahn (2016) and
57 references therein), as well as the broader literature looking at mid-latitude
58 extremes (e.g. Von Storch and Zwiers (2001); Coumou et al (2014); Palmer
59 (2013); Gálfi et al (2017)). These point to the degree of coupling between
60 atmospheric circulation variables and temperature as a key step to both un-
61 derstand the physical drivers of the extremes and constrain the variability
62 of climate models in order to better simulate such events in future climates.
63 Specifically, we diagnose the dynamical features and coupling of the sea-level
64 pressure (SLP) and 2-m temperature (T2M) fields in reference to the above-
65 mentioned North American temperature extremes. The purpose is to provide
66 a proof-of-concept for the applicability of our novel analysis approach - which

is entirely general and may in theory be extended to any number of variables - to the study of multi-variate atmospheric configurations.

We begin by providing a theoretical definition of three dynamical systems metrics: d , θ^{-1} and α . The local dimension d can be intuitively interpreted as a proxy for the number of active degrees of freedom of the system around a given state. The persistence θ^{-1} measures the residence time around such state. Finally, the coupling parameter (also referred to as co-recurrence ratio) α informs on the dependence structure between instantaneous configurations of different variables. We next test these metrics on simple stochastic processes and discrete dynamical systems. Following this, we apply our framework to study the drivers underlying the occurrence of temperature extremes in North America.

2 Dynamical systems indicators

The attractor of a dynamical system is a geometrical object defined in the space hosting all the possible states of the system (phase-space). For atmospheric flows, it is unfeasible to obtain all *variables* of the system, as this would require the knowledge of the properties of each fluid parcel. What is instead available is a set, or sequences, of *observables* — namely transformations of the variables of the system. By making some assumptions on the dimensionality of the system, it is possible to retrieve its entire dynamics from the observables (Huke, 2006). This allows the computation of the fractal dimension of the system (Grassberger, 1983; Grassberger and Procaccia, 1984). The major caveat of such approaches lies in the underlying mathematical assumptions, that render the application to geophysical datasets problematic (Eckmann and Ruelle, 1992). Recently, an alternative approach to determine a system’s dynamical properties has been proposed, which does not require a priori assumptions on the dimensionality of the system. This approach is based on an analysis of the recurrences of trajectories of the dynamical system, and has been successfully tested on various complex datasets (Faranda et al, 2017a,b). One of the outcomes is a characterization of each point ζ of this subset of variables by two dynamical indicators: the local dimension (d) and the persistence (θ^{-1}) (Faranda et al, 2017b). There have been theoretical (Barros et al, 2019) and experimental (Faranda et al, 2017a,c) arguments that show that recurrences of observables yield the same behavior as the underlying variables.

We consider a dynamical system with an observed trajectory $x(t)$ and a point in phase space ζ . We are interested in the behavior of the system near ζ . Therefore a logarithmic return is defined as:

$$g(x(t), \zeta) = -\log[\text{dist}(x(t), \zeta)]. \quad (1)$$

This transformation gives weight to parts of the trajectory $x(t)$ that are close to ζ , i.e. when the distance is close to 0. Given $s(q, \zeta)$ a high q -th quantile of the time series of $g(x(t), \zeta)$, we introduce the exceedances $u(\zeta) =$

107 $g(x(t), \zeta) - s(q, \zeta)$ with the condition $g(x(t), \zeta) > s(q, \zeta)$. The cumulative prob-
 108 ability distribution of $F(u, \zeta)$ then converges to the exponential member of the
 109 Generalized Pareto Distribution (Freitas et al, 2010; Lucarini et al, 2012):

$$F(u, \zeta) \simeq \exp \left[-\theta(\zeta) \frac{u(\zeta)}{\sigma(\zeta)} \right]. \quad (2)$$

110 The parameters θ and σ depend on the point ζ chosen on the attractor. As
 111 discussed below, θ and σ are fundamental quantities to describe the dynamical
 112 properties of the system.

113 2.1 Local dimension

114 The local dimension $d(\zeta)$ is obtained via the simple relation $d(\zeta) = 1/\sigma(\zeta)$.
 115 This result holds when $x(t)$ contains the system's full set of phase-space vari-
 116 ables. In this case, d is independent of the chosen dist for all ζ . If $x(t)$ is
 117 an *observable* of the system, i.e. some smooth function of a variable in the
 118 full phase space, such as a 2-dimensional atmospheric field, $d(\zeta)$ can still be
 119 computed in this way (Rousseau and Saussol, 2010; Rousseau, 2014), but the
 120 quantitative results will depend on the distance definition.

121 In principle, the results are insensitive to the choice of the distance in
 122 the asymptotic limit. For practical reasons, we use the L^2 norm or Euclidean
 123 distance, which is also used to compute circulation analogues (e.g. Yiou et al
 124 (2013)). We also emphasize that the value of d is bounded by the number of
 125 coordinates of the observable and the dynamics of the system.

126 Given two observables (or two sets of observables) $x(t)$ and $y(t)$ of a
 127 "larger" system, we can define $d_x(\zeta)$ and $d_y(\zeta)$ (from now on we will drop
 128 the dependence on ζ). They are the dimensions of the Poincaré sections de-
 129 fined by x and y around ζ , with respect to the chosen dist. We can further
 130 consider the Poincaré section jointly spanned by x and y . A state on this sec-
 131 tion is then defined by the pair $\zeta = \{\zeta_x, \zeta_y\}$. The joint logarithmic returns can
 132 then be defined as:

$$g(x(t), y(t)) = -\log \left[\text{dist} \left(\frac{x(t)}{\|x\|}, \frac{\zeta_x}{\|\zeta_x\|} \right)^2 + \text{dist} \left(\frac{y(t)}{\|y\|}, \frac{\zeta_y}{\|\zeta_y\|} \right)^2 \right]^{\frac{1}{2}} \quad (3)$$

133 Here, $\|\cdot\|$ is the average root mean square norm of the coordinates of a
 134 vector. For example, $\|x\| = E_t \left(\left[\sum_i^K x_i(t)^2 \right]^{\frac{1}{2}} \right)$, where K is the number of
 135 components of x and E_t is an average over time t . Based on Eq. (3), we call
 136 $d_{x,y}$ the *co-dimension* between x and y .

137 The co-dimension can be used as a first quantity to characterise the mutual
 138 dependence of two observables. For two observables x and y of the system, the
 139 following properties hold:

$$\min(d_x, d_y) \leq d_{x,y} \leq d_x + d_y \quad (4)$$

140 If x and y are uncoupled, then $d_{x,y} = d_x + d_y$. If x and y are determinis-
 141 tically coupled (e.g. one is a function of the other), then $d_{x,y} = \min(d_x, d_y)$.
 142 We exemplify these behaviours for a discrete dynamical system in Sec. 3.2.

143 2.2 Local persistence

144 The persistence of the state ζ is measured by $\theta(\zeta)$. θ is known as the extremal
 145 index. In our setup, it corresponds to the inverse of the average residence time
 146 of trajectories around ζ . Since θ is the inverse of the average residence time, it
 147 is measured in units of $1/\Delta t$. If ζ is a fixed point of the attractor then $\theta(\zeta) = 0$
 148 (trajectories stay at ζ). For a point that immediately leaves the neighborhood
 149 of ζ , then $\theta = 1$. Intermediate values of θ are obtained for regions of the
 150 attractor that are close to fixed points, and that trajectories leave "slowly".
 151 To estimate θ , we adopt the Süveges estimator (Süveges, 2007).

152 As for d above, the procedure can be extended to more than one variable,
 153 such that one may define the inverse co-persistence $\theta_{x,y}$. The values of the
 154 inverse co-persistence depend on the local topology of the different Poincaré
 155 sections being considered. $\theta_{x,y}$ is a weighted average of θ_x and θ_y where the
 156 weights depend on the size of the hyper-ball around ζ in the Poincaré sections
 157 x and y . For a more detailed discussion we refer the reader to Abadi et al
 158 (2018).

159 2.3 Local co-recurrence ratio

160 Given two observables x and y , we define the co-recurrence ratio $0 \leq \alpha(\zeta) \leq 1$
 161 of a state $\zeta = \{\zeta_x, \zeta_y\}$ as:

$$\alpha(\zeta) = \frac{\Pr[g(x(t)) > s_x(q) | g(y(t)) > s_y(q)]}{\Pr[g(x(t)) > s_x(q)]} \quad (5)$$

162 that is, the probability of entering a hyper-ball in phase space around
 163 $\zeta = \{\zeta_x, \zeta_y\}$ divided by the probability of entering the ball centered in ζ_x
 164 only. Whenever x and y do not have the same units, a normalization $x/\|x\|$
 165 and $y/\|y\|$ must be performed before computing α . When $\alpha(\zeta) = 0$, there are
 166 no co-recurrences of $\zeta = \{\zeta_x, \zeta_y\}$ when we observe a recurrence of ζ_x . When
 167 $\alpha(\zeta) = 1$, all the co-recurrences of $\zeta = \{\zeta_x, \zeta_y\}$ also correspond to recurrences
 168 of ζ_x .

169 Here, we have defined α in the case of two variables x and y , but the
 170 approach can easily be extended to more complex multivariate cases. From
 171 Bayes' theorem on conditional probabilities, we note that α does not depend
 172 on the order of x and y , which can hence be exchanged. This implies that α
 173 cannot be interpreted in terms of causation. We further note that α is not
 174 necessarily correlated with the co-dimension $d_{x,y}$, as discussed further in Sect

175 3.2. Finally, we underscore that α cannot be directly compared to statistical
 176 dependence measures because of its local nature in phase space.

177 3 Application to stochastic processes and dynamical systems

178 3.1 Gaussian Bivariate copula

179 To illustrate the interpretation of α , we draw data from random Gaussian
 180 bivariate copula distributions, namely:

$$\phi(z, \mu, \Sigma) = \frac{1}{\sqrt{4\pi^2|\Sigma|}} \exp\left[-\frac{1}{2}(z - \mu)' \Sigma^{-1}(z - \mu)\right] \quad (6)$$

181 where $z = (x, y)$ is an i.i.d. variable vector in $[0, 1] \times [0, 1]$, μ is the mean
 182 vector, Σ is a 2×2 symmetric matrix and $|\Sigma|$ is its norm. The diagonal elements
 183 of Σ contain the variances for each variable (x, y) , while the off-diagonal
 184 elements of Σ contain the covariances between variables (x, y) . In the example
 185 we set $\mu = \{0, 0\}$ and the diagonal elements of Σ equal to one. We term the
 186 non-diagonal elements ρ .

187 By varying ρ , we can obtain a range of different types of behaviour. There
 188 are two extreme cases: for $\rho = 0$, $\{x, y\}$ cover uniformly the unit square; for
 189 $\rho = 1$, $x = y$ and data are aligned along the first diagonal. We illustrate
 190 graphically four different cases: $\rho = 0.5$, $\rho = 0.75$, $\rho = 0.9992$, and $\rho = 1$. We
 191 generate 10^5 values of z for each case. For clarity we report 2×10^3 points
 192 in Figure 1. These are colored by the values of α , the co-recurrence ratio,
 193 computed by fixing the quantile $q = 0.98$.

194 The behavior of α is somewhat intuitive: when the variables are locally
 195 independent (Figure 1a-b), $\alpha = 0$ almost everywhere. When ρ is close to 1
 196 (Figure 1c), near the edges $(0,0)$ and $(1,1)$ the dependence is very strong and
 197 $\alpha=1$. Near the centre $(x = y = 0.5)$ the dependence is lower and $\alpha < 1$. This
 198 behavior is determined by the very nature of the distribution considered here,
 199 which is constrained to be close to the diagonal near the edge points. In the
 200 perfect coupling case $\rho = 1$ (Figure 1d), $x = y$ and $\alpha = 1$ along the full length
 201 of the diagonal.

202 3.2 The baker's map

203 To further illustrate the properties of the dynamical indicators, we analyse a
 204 modified version of the baker's map, defined on the unit square $[0, 1] \times [0, 1]$
 205 iteratively for $n \geq 1$, by:

$$x_{n+1} = \begin{cases} ax_n, & \text{for } y_n < c \\ \frac{1}{2} + bx_n, & \text{for } y_n > c \end{cases} \quad (7)$$

206 and

$$y_{n+1} = \begin{cases} y_n/a, & \text{for } y_n < c \\ (y_n - c)/(1 - c), & \text{for } y_n > c \end{cases} \quad (8)$$

207 with $c = 1/3$, $a = 1/5$ and $b = 1/4$. For these parameters values, the map is
 208 expanding on x and contracting on y . Figure 2-a shows the first 10^5 iterations
 209 of the map. Along the x direction, the map consists of a fractal set where
 210 $d_x < 1$ while along y there is an uncountable collection of lines with $d_y = 1$.
 211 We can add coupling between x and y as:

$$x_{n+1} = (1 - \epsilon)x_n + \epsilon y_n.$$

212 with $0 \leq \epsilon \leq 1$. When ϵ is zero, x and y are uncoupled. As ϵ increases, the
 213 dynamics of x, y becomes more and more synchronized. Finally, when $\epsilon = 1$,
 214 the dynamics is synchronized and concentrated on the diagonals (Figure 2-b).

215 To illustrate the properties of the co-dimension and the co-recurrence co-
 216 efficients in this set-up, we change the values of ϵ in the range $10^{-10} < \epsilon < 1$
 217 and perform 10^6 iterations of the maps starting from random initial conditions
 218 on the unit square. The first 10^4 iterations are discarded. We then compute
 219 the dynamical indicators at 500 points ζ . Figure 3 shows the results of this
 220 computation for d_x , d_y , $d_{x,y}$ and α . In the limit $\epsilon \rightarrow 0$, $d_x + d_y = d_{x,y}$ and
 221 $\alpha \simeq 0$. When increasing the coupling $d_{x,y} < d_x + d_y = 2$. In the limit for
 222 $\epsilon = 1$, $x \propto y$, $d_{x,y} = 1$ and α approaches 1. This simple example highlights the
 223 different information provided by the co-dimension and co-recurrence ratio. In-
 224 deed, the co-dimension generally decreases for increasing coupling, while the
 225 co-recurrence ratio increases. We further note that the co-recurrence ratio pro-
 226 vides a normalised dependence measure, while the value of the co-dimension
 227 depends on the relative dimension on the x and y manifold. The behavior for
 228 θ is not shown as, for this system, we have trivially that $\theta_x = \theta_y = \theta_{x,y}$ for all
 229 ϵ .

230 4 Application to North American temperature extremes

231 4.1 Data and Methods

232 We base our study on NCEP/NCAR reanalysis data (Kalnay et al, 1996) over
 233 the period 1948-2015, with a horizontal resolution of 2.5° . We consider a do-
 234 main spanning North America ($170^\circ\text{W} \leq \text{Long.} \leq 40^\circ\text{W}$, $22.5^\circ\text{N} \leq \text{Lat.} \leq 70^\circ\text{N}$).
 235 We adopt daily SLP as the meteorological variable to describe the large scale
 236 atmospheric circulation. Indeed, a wealth of atmospheric features, ranging
 237 from teleconnection patterns to storm track activity to atmospheric blocking
 238 can be diagnosed from the SLP field (e.g. Murray and Simmonds (1991); Yiou
 239 et al (2013); Comas-Bru and McDermott (2014)).

240 Warm and cold days and temperature quantiles are diagnosed using area-
 241 weighted, daily T2M anomalies over land points in $100^\circ\text{W} \leq \text{Long.} \leq 70^\circ\text{W}$, and
 242 $30^\circ\text{N} \leq \text{Lat.} \leq 45^\circ\text{N}$, corresponding to a densely populated part of western North
 243 America (see Figure 4). The anomalies are computed analogously to Messori
 244 et al (2016), and specifically by imposing a separation of one week between suc-
 245 cessive warm or cold extremes. We consider winter (DJF) and summer (JJA)
 246 seasons separately. The warm and cold day quantiles are computed relative

247 to all days with positive and negative temperature anomalies, respectively,
 248 after the minimum separation criterion has been applied. We refer to these
 249 throughout the text as *warm days* and *cold days* respectively.

250 All the geographical plots display single-gridpoint anomalies relative to a
 251 daily seasonal cycle, defined by averaging all days available in the dataset. For
 252 example, the climatological value at a given gridbox for the 3rd December is
 253 the average value at that gridbox for all 68 3rd Decembers in the data.

254 4.2 Dynamical properties and seasonality

255 We analyse the relations between local dimension d , persistence θ^{-1} and co-
 256 recurrence ratio α for SLP and T2M. We consider the cases where d and
 257 θ are computed on each variable individually and on both variables at the
 258 same time. α is naturally always computed on both variables. The results
 259 are reported in Figure 5 in the form of dimension-persistence diagrams, as
 260 introduced in Faranda et al (2017b). Each point in the diagram represents
 261 a pair (d, θ) corresponding to the patterns observed on a given day for the
 262 variable(s) of interest. The colorscale shows the values of α .

263 α is negatively correlated with d_{SLP} (Figure 5a), meaning that configu-
 264 rations with lower d typically favour a higher coupling. The fact that d and
 265 θ are themselves correlated implies that the latter configurations are, on av-
 266 erage, also highly persistent. The picture for T2M is less clear (Figure 5b):
 267 strongly coupled states often correspond to high d and low-persistence con-
 268 figurations. Finally, the joint analysis highlights a similar pattern as for SLP,
 269 with α showing a clear dependence on the co-dimension $d_{SLP,T2M}$.

270 Faranda et al (2017a) found that the correlations evident in dimension-
 271 persistence diagrams, as those shown in Figure 5, reflected the strong seasonal
 272 dependence of the metrics. We therefore investigate the seasonal cycle in the
 273 above quantities (Figure 6). All three indicators are subject to a marked sea-
 274 sonality, with α presenting a clear peak in summertime, when mean values are
 275 more than twice those of the rest of the year. The local dimension d instead
 276 displays maxima in the shoulder seasons for SLP, and minima for T2M. The
 277 variability is not, however, as marked as that seen in α . The co-dimension
 278 $d_{SLP,T2M}$ does not follow the seasonal cycle of either d_{SLP} or d_{T2M} . It peaks
 279 in late spring/early summer and early autumn, while displaying mid-summer
 280 and winter minima. θ_{SLP} is mostly in phase with d_{SLP} , as is θ_{T2M} with d_{T2M} ,
 281 although the relative magnitude of the summer and winter peaks is inverted.
 282 The inverse co-persistence $\theta_{SLP,T2M}$ again does not follow either of the single-
 283 variable cycles, but rather displays an oscillatory behavior throughout the
 284 year, somewhat reminiscent of the variability in $d_{SLP,T2M}$. The largest values
 285 tend to occur during the autumn and winter months, while the lowest values
 286 are mostly found in spring.

287 The seasons during which most of the highest and lowest values of the
 288 three indicators occur are coherent with these seasonal cycles (Figure 7). Even
 289 though the mean of α has a very clear summertime peak, the fact that the

290 variability peaks instead in winter (Figure 6a) implies that a small number of
 291 α maxima are seen during this season. This matches the timing of minima in
 292 both d_{SLP} and θ_{SLP} , consistent with what shown in Figure 5a. The α minima
 293 occur instead predominantly in spring, when d_{SLP} and θ_{SLP} display relatively
 294 large values. Similar conclusions can be drawn concerning the co-dimension
 295 and co-persistence (Figure 7).

296 This highlights a clear separation between seasons. The most striking fea-
 297 ture is the above-mentioned seasonality in α , with distinct wintertime and
 298 summertime behaviours. In order to investigate further the physical interpre-
 299 tation of coupling minima and maxima, we therefore analyse these two seasons
 300 separately.

301 4.3 Temperature extremes

302 The above results show that d , θ and α display both a large variability and
 303 a strong seasonal dependence. This is explained by the very different fea-
 304 tures of atmospheric dynamics found in the different seasons (see Faranda
 305 et al (2017a)), and shifts between predominantly baroclinic and predominantly
 306 barotropic flows. Even though the mean values of the metrics and an analysis
 307 of their seasonal variability can provide interesting physical insights, such as
 308 assessing which seasons present more or less coupling in SLP and temperature,
 309 the real added value in having instantaneous metrics is the possibility of using
 310 them to study the dynamics of meteorological extremes. Here, we use the three
 311 dynamical systems metrics to investigate warm and cold extremes over North
 312 America, during both the summer(JJA) and winter (DJF) seasons.

313 *Summer extremes.* We begin by considering summertime warm and cold days
 314 (see Section 4.1). The co-dimension and co-persistence, as a function of the
 315 temperature quantile over the selection domain, show no clear change for ex-
 316 treme warm and extreme cold events relative to their respective seasonal cycles
 317 (Figure 8a,b). Similarly, α (Figure 8c) remains close to its seasonal cycle, re-
 318 gardless of the temperature quantile. This points to the fact that the joint d
 319 and θ metrics do not reflect the evolution of the temperature field and that,
 320 consistently with this, the co-recurrence ratio is also largely insensitive to tem-
 321 perature extremes. The d and θ metrics computed for the SLP and T2M fields
 322 individually (Figure 8a,b) display a similar behaviour, except for some larger
 323 deviations of d from the seasonal cycle for the most extreme quantiles.

324 To highlight the link between the dynamical systems metrics and the un-
 325 derlying physical properties of the atmospheric circulation associated with
 326 different events, we define an average daily baroclinic vector:

$$B = \overline{\nabla(SLP) \times \nabla(T2M)} \quad (9)$$

327 where the overbar symbolises a spatial mean over the domain highlighted
 328 in black in Figure 4. Values close to zero indicate a predominantly barotropic

329 atmosphere i.e. the isolines of pressure are aligned with those of tempera-
 330 ture. Positive and negative values correspond instead to warm and cold air
 331 advection, respectively. The caveat is that we do not account for cancellation
 332 between opposing advectons in the domain. Average values for B are shown
 333 in Figure 8d). In this season, all the values of B are generally close to zero (the
 334 weakly positive values for the cold anomalies reflect the decoupling between
 335 SLP and T2M discussed above). This decoupling is also reflected in the T2M
 336 and SLP composites for α extremes: the anomalies are weak throughout the
 337 domain, and the sign agreement between the different extreme α occurrences
 338 is low (Figure 9).

339 *Winter extremes.* The situation in winter is radically different: $d_{SLP,T2M}$,
 340 $\theta_{SLP,T2M}$ and α all show significant deviations from the climatology for the
 341 higher quantiles of the hot and cold day samples. These are roughly opposite,
 342 with cold extremes showing negative d and θ deviations and warm extremes
 343 showing positive anomalies (Figure 10a-b). The d and θ computed for the two
 344 variables individually show a similar behaviour, although for the case of T2M
 345 and warm events the deviations from the seasonal cycle are smaller than for the
 346 joint metrics and generally not significant (Figure 10a-b). The co-recurrence
 347 ratio also shows deviations of the opposite sign: negative for warm extremes
 348 and positive for cold extremes (Figure 10c). The analysis of the baroclinic
 349 vector B (Figure 10d) provides here clear insights on such asymmetry: cold
 350 extremes correspond to a strong cold advection ($B < 0$), while the warm ex-
 351 tremes display a weaker warm advection and positive B . This reflects very
 352 closely the behaviour of the coupling coefficient α .

353 By conditioning purely on low and high values of α , one recovers strong
 354 temperature anomalies over the domain of interest, associated with anomalous
 355 SLP patterns favoring strong meridional advection (Figure 11). The SLP
 356 and T2M fields therefore appear to display recurring joint large-scale config-
 357 urations which favour both classes of temperature extremes. This may seem
 358 in contradiction with the information provided by α as one may expect no
 359 coherent large scale SLP patterns to be associated with α minima (and hence
 360 warm extremes). We expand on this aspect in the discussion section.

361 5 Discussion and conclusions

362 We have proposed two metrics to diagnose the properties of instantaneous
 363 configurations of atmospheric variables, namely local dimension d and inverse
 364 persistence θ . The first is a proxy for the number of active degrees of freedom of
 365 a given configuration, while the second measures the average time over which a
 366 configuration is maintained. These indicators have been previously applied to
 367 individual atmospheric variables (Faranda et al, 2016, 2017b,a; Messori et al,
 368 2017; Rodrigues et al, 2018); here, we present their use in a multi-variate con-
 369 text. Specifically, we compute d and θ jointly for sea-level pressure (SLP) and
 370 2-metre temperature (T2M) over North America. We further introduce a novel

metric which measures the co-occurrence of analogue states of multiple variables: the co-recurrence ratio α . A small α indicates rare co-recurrences, while a large α indicates that recurrences of a given state in one of the two variables systematically match recurrences of a corresponding state in the other. This metric provides an important piece of information, as it elucidates the mutual dependence between the dynamical evolutions of the two variables. Indeed, unlike statistical dependence measures, α is grounded in the topology of the variables' phase-space, and therefore in the local geometry of the underlying attractor. Locality in phase space, which translates to simultaneity in time, makes the above framework well-suited to the study of atmospheric variability and extremes.

As an illustration, we have investigated the occurrence of cold or hot days in North America, linking temperature anomalies over the eastern part of the continent to the larger-scale T2M and SLP fields. We identify strongly and weakly coupled states in these two variables and then elucidate the interplay between these and the occurrence of the temperature extremes.

Summertime temperature extremes appear to be unrelated to the joint dynamical properties of the two selected large-scale fields. This is also reflected in the d and θ metrics computed on the individual variables and in the weak co-recurrence between SLP and T2M. The recurrences of SLP anomaly fields associated with temperature extremes are not matched by recurrences of the same T2M anomaly fields, or at least not more so than what is typical for any day in the summer season. Indeed, both the sign agreement and magnitude of the large-scale SLP anomalies associated with the hot and cold temperature extremes are relatively weak and display very limited sign agreement (see Fig. 12 for the upper/lower 10 percentiles). Similarly, a proxy for temperature advection shows near-zero values (B in Fig. 8d). This points to local factors, not captured by the large-scale SLP field analysed here as contributors to these events (e.g. local soil moisture anomalies, small-scale precipitation events, local sensible heat fluxes etc.).

In winter, the picture is different (see Fig. 13 for the SLP anomalies corresponding to the upper/lower 10 percentiles of T2M). Both the joint and individual d and θ discriminate hot and cold extremes, and these also display anomalous α values. Cold extremes are characterised by an anomalously high persistence, low local dimension and strong coupling. This points to the need for persistent circulation patterns and large-scale cold advection (Fig 11d) for a cold spell to occur, as well as to the fact that whenever cold spells occur, similar large-scale T2M and SLP patterns are found (Cellitti et al, 2006; Grotjahn, 2016; Walsh et al, 2001; Messori et al, 2016). Here we identify these as: a large anticyclone over North America, advecting cold, dry air from the Arctic region (as reflected by the baroclinic vector B (Figure 10d), and two low-pressure cores on either flank. Such pattern leads to widespread low temperatures as far south as Texas and Northern Florida. Warm extremes are instead characterised by an anomalously low persistence, high local dimension and low coupling. The deviations from the seasonal cycle are also smaller in magnitude than for the case of the cold extremes. The large-scale pattern is

roughly inverse to that seen for the cold spells, with a cyclonic anomaly over the continent favouring advection of warm, moist air from the low latitudes (Figure 10d and Figure 11d) and leading to high temperatures on the eastern seaboard of the US and Canada. The transient nature of this cyclonic advection is reflected in the anomalously low persistence and high local dimension which, as seen in Fig.5c, correspond to low α values.

There is an evident ambiguity in an apparently coherent large scale anomalous SLP pattern and the claim of a weak coupling to the T2M field. A possible explanation is that the dynamical systems analysis is performed on the absolute fields rather than on the anomalies as shown in the figures. Since the co-recurrence ratio is sensitive to the seasonal cycle (Figure 6a), this may introduce a discrepancy between absolute and anomalous recurrence patterns. This points to the need to perform a systematic analysis on the anomalous fields although this is far from trivial in a dynamical systems context. Indeed there is no currently accepted framework for removing the average attractor components and then characterising the residual fluctuations. Formally, this would correspond to analysing recurrences within hyper-ellipsoids where the eccentricity depends on the position in phase space rather than hyper-spheres.

The above analysis has shown some of the insights that can be provided by our local (in phase-space, instantaneous in time) and multi-variate dynamical systems analysis as well as some ongoing challenges. As such, it should be viewed as a proof of concept for the validity of this approach. More generally, there is no requirement for the different variables to be geographically co-located or temporally coincident, as was the case here. For example, one could select SLP over a region upstream of the target temperature region, or could use SLP fields lagged by a few days relative to the T2M data. Similarly, our approach can be generalised to higher dimensional variables or to a larger number of variables. The technique is entirely flexible, and is immediately applicable to observables of any complex system.

Acknowledgements DF, PY and GM acknowledge the support of the ERC grant No. 338965-A2C2. GM was supported by a grant from the Department of Meteorology of Stockholm University and by Swedish Research Council grant No. 2016-03724.

References

- Abadi M, Freitas ACM, Freitas JM (2018) Dynamical counterexamples regarding the extremal index and the mean of the limiting cluster size distribution. arXiv preprint arXiv:180802970
- Barros V, Liao L, Rousseau J (2019) On the shortest distance between orbits and the longest common substring problem. *Advances in Mathematics* 344:311–339
- Bevacqua E, Maraun D, Hobæk Haff I, Widmann M, Vrac M (2017) Multivariate statistical modelling of compound events via pair-copula constructions:

- 458 analysis of floods in ravenna (italy). *Hydrology and Earth System Sciences*
459 21(6):2701–2723
- 460 Cellitti MP, Walsh JE, Rauber RM, Portis DH (2006) Extreme cold air out-
461 breaks over the united states, the polar vortex, and the large-scale circula-
462 tion. *Journal of Geophysical Research: Atmospheres* 111(D2)
- 463 Comas-Bru L, McDermott F (2014) Impacts of the ea and sca patterns on
464 the european twentieth century nao–winter climate relationship. *Quarterly*
465 *Journal of the Royal Meteorological Society* 140(679):354–363
- 466 Coumou D, Petoukhov V, Rahmstorf S, Petri S, Schellnhuber HJ (2014) Quasi-
467 resonant circulation regimes and hemispheric synchronization of extreme
468 weather in boreal summer. *Proceedings of the National Academy of Sciences*
469 111(34):12,331–12,336
- 470 Davies HC (2015) Weather chains during the 2013/2014 winter and their sig-
471 nificance for seasonal prediction. *Nature Geoscience* 8(11):833
- 472 Eckmann JP, Ruelle D (1992) Fundamental limitations for estimating dimen-
473 sions and lyapunov exponents in dynamical systems. *Physica D: Nonlinear*
474 *Phenomena* 56(2-3):185–187
- 475 Faranda D, Masato G, Moloney N, Sato Y, Daviaud F, Dubrulle B, Yiou
476 P (2016) The switching between zonal and blocked mid-latitude atmo-
477 spheric circulation: a dynamical system perspective. *Climate Dynamics*
478 47(5-6):1587–1599
- 479 Faranda D, Messori G, Alvarez-Castro MC, Yiou P (2017a) Dynamical prop-
480 erties and extremes of northern hemisphere climate fields over the past 60
481 years. *Nonlinear Processes in Geophysics* 24(4):713
- 482 Faranda D, Messori G, Yiou P (2017b) Dynamical proxies of north atlantic
483 predictability and extremes. *Scientific reports* 7:41,278
- 484 Faranda D, Sato Y, Saint-Michel B, Wiertel C, Padilla V, Dubrulle B, Daviaud
485 F (2017c) Stochastic chaos in a turbulent swirling flow. *Physical review*
486 *letters* 119(1):014,502
- 487 Freitas ACM, Freitas JM, Todd M (2010) Hitting time statistics and extreme
488 value theory. *Probab Theor Rel* 147(3-4):675–710
- 489 Galambos J, Lechner J, Simiu E, Hagwood C (1994) Extreme value theory for
490 applications:. NIST technical publications
- 491 Gálfi VM, Bódai T, Lucarini V (2017) Convergence of extreme value statistics
492 in a two-layer quasi-geostrophic atmospheric model. *Complexity* 2017
- 493 Gnedenko B (1943) Sur la distribution limite du terme maximum d’une serie
494 aleatoire. *Annals of mathematics* pp 423–453
- 495 Grassberger P (1983) Generalized dimensions of strange attractors. *Physics*
496 *Letters A* 97(6):227–230
- 497 Grassberger P, Procaccia I (1984) Dimensions and entropies of strange attrac-
498 tors from a fluctuating dynamics approach. *Physica D: Nonlinear Phenom-*
499 *ena* 13(1-2):34–54
- 500 Grotjahn R (2016) Western north american extreme heat, associated large
501 scale synoptic-dynamics, and performance by a climate model. *Dynamics*
502 *and Predictability of Large-Scale, High-Impact Weather and Climate Events*
503 2:198

- 504 Harnik N, Messori G, Caballero R, Feldstein SB (2016) The circumglobal
505 north american wave pattern and its relation to cold events in eastern north
506 america. *Geophysical Research Letters* 43(20)
- 507 Huke J (2006) Embedding nonlinear dynamical systems: A guide to taken's
508 theorem
- 509 Kalnay E, Kanamitsu M, Kistler R, Collins W, Deaven D, Gandin L, Iredell M,
510 Saha S, White G, Woollen J, et al (1996) The ncep/ncar 40-year reanalysis
511 project. *B Am Meteorol Soc* 77(3):437–471
- 512 Lucarini V, Faranda D, Wouters J (2012) Universal behaviour of extreme value
513 statistics for selected observables of dynamical systems. *Journal of statistical
514 physics* 147(1):63–73
- 515 Messori G, Caballero R, Gaetani M (2016) On cold spells in north america and
516 storminess in western europe. *Geophysical Research Letters* 43(12):6620–
517 6628
- 518 Messori G, Caballero R, Faranda D (2017) A dynamical systems approach
519 to studying midlatitude weather extremes. *Geophysical Research Letters*
520 44(7):3346–3354
- 521 Murray RJ, Simmonds I (1991) A numerical scheme for tracking cyclone centres
522 from digital data. *Australian Meteorological Magazine* 39(3):155–166
- 523 Palmer T (2013) Climate extremes and the role of dynamics. *Proceedings of
524 the National Academy of Sciences* 110(14):5281–5282
- 525 Pickands III J (1975) Statistical inference using extreme order statistics. *the
526 Annals of Statistics* pp 119–131
- 527 Rodrigues D, Alvarez-Castro MC, Messori G, Yiou P, Robin Y, Faranda D
528 (2018) Dynamical properties of the north atlantic atmospheric circulation
529 in the past 150 years in cmip5 models and the 20crv2c reanalysis. *Journal
530 of Climate* (2018)
- 531 Rousseau J (2014) Hitting time statistics for observations of dynamical systems.
532 *Nonlinearity* 27(9):2377
- 533 Rousseau J, Saussol B (2010) Poincaré recurrence for observations. *Transactions
534 of the American Mathematical Society* 362(11):5845–5859
- 535 Süveges M (2007) Likelihood estimation of the extremal index. *Extremes* 10(1-
536 2):41–55
- 537 Von Storch H, Zwiers FW (2001) *Statistical analysis in climate research*. Cambridge
538 university press
- 539 Walsh JE, Phillips AS, Portis DH, Chapman WL (2001) Extreme cold
540 outbreaks in the united states and europe, 1948–99. *Journal of climate*
541 14(12):2642–2658
- 542 Yiou P, Salameh T, Drobinski P, Menut L, Vautard R, Vrac M (2013) Ensemble
543 reconstruction of the atmospheric column from surface pressure using
544 analogues. *Climate dynamics* 41(5-6):1333–1344
- 545 Zscheischler J, Seneviratne SI (2017) Dependence of drivers affects risks associated
546 with compound events. *Science Advances* 3(6):e1700,263

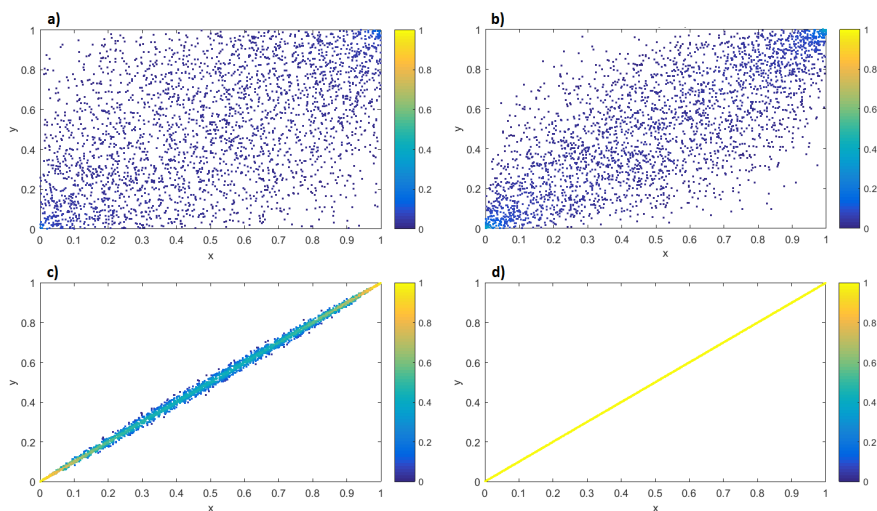


Fig. 1 Four different realizations of the Gaussian bivariate copula (Eq. 6) with $\rho = 0.5$ (a), $\rho = 0.75$ (b), $\rho = 0.9992$ (c), $\rho = 1$ (d). The co-recurrence ratio α is displayed in color.

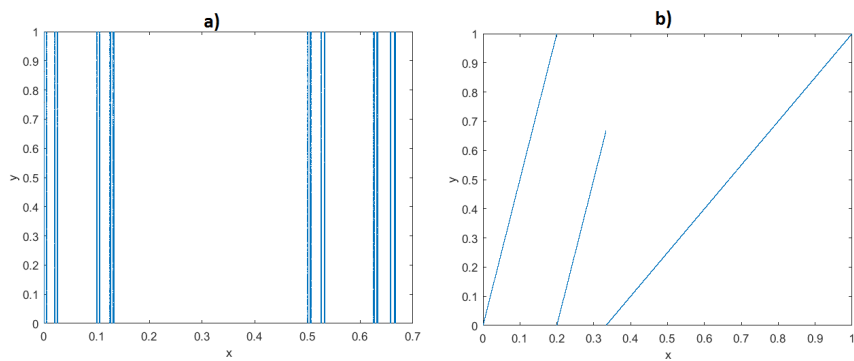


Fig. 2 Two different realizations of 10^5 iterations of the baker's map (Eq. 8) with $\epsilon = 0$ (a), and $\epsilon = 1$ (b).

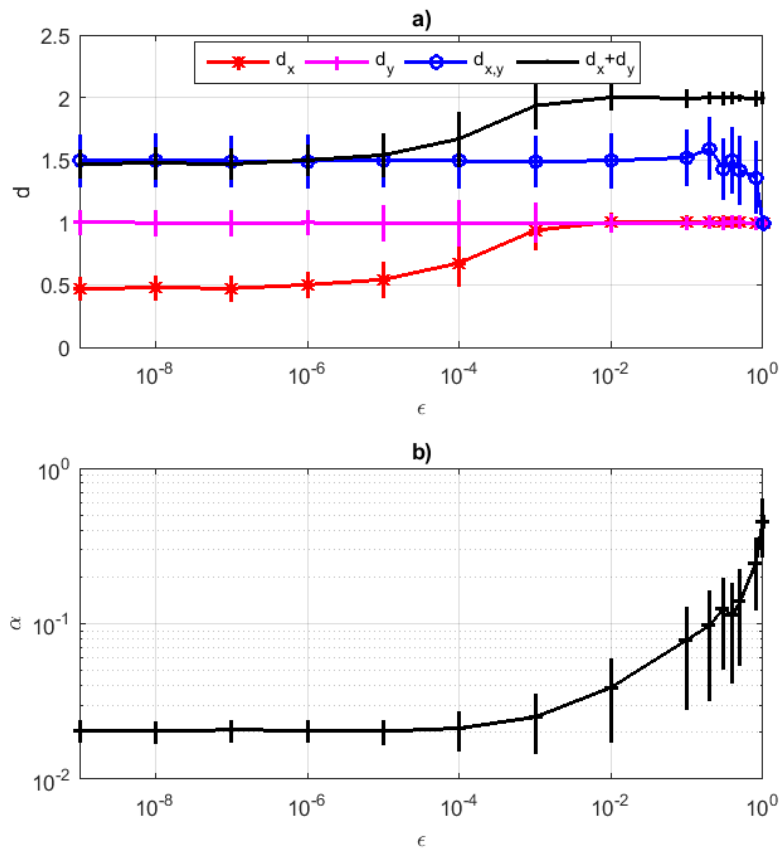


Fig. 3 Dynamical indicators for the baker's map (Eq. 8). a) Dimensions d_x and d_y and co-dimensions $d_{x,y}$ compared to $d_x + d_y$ for different values of ϵ . b) Co-recurrence ratio α for different values of ϵ . Error bars show 1 standard deviation of the d, α distributions.

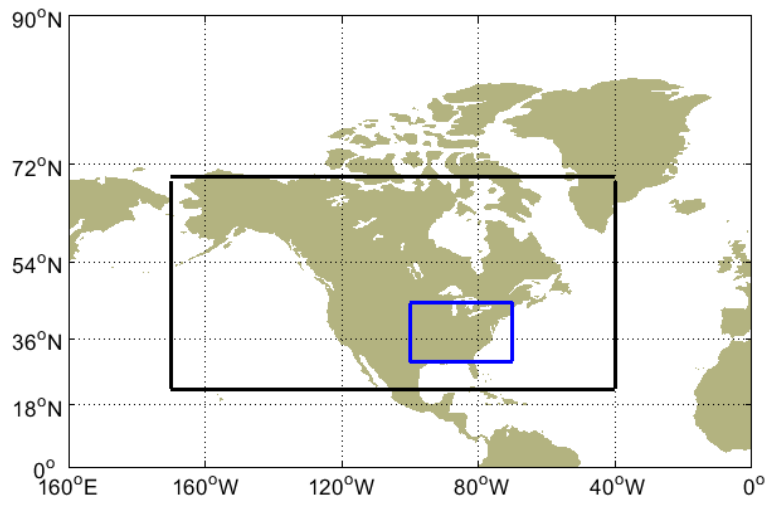


Fig. 4 The region studied in this article. The black rectangle highlights the domain over which the dynamical indicators are computed; the blue rectangle highlights the domain over which the temperature extremes are computed.

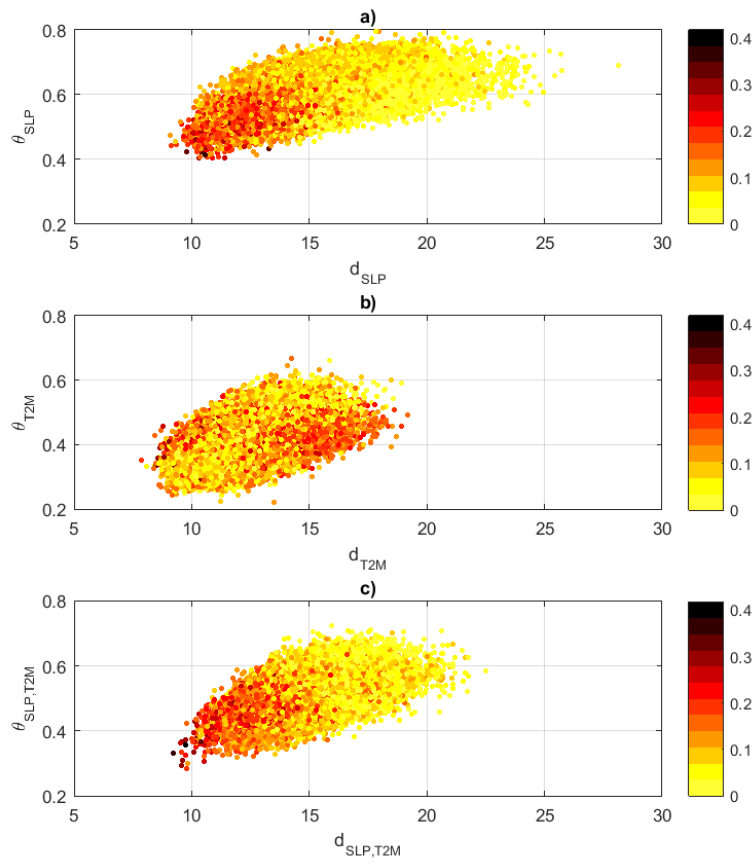


Fig. 5 Local dimension d and inverse persistence θ scatter plots colored with the values of the co-recurrence ratio α . a) d_{SLP} and θ_{SLP} . b) d_{T2M} and θ_{T2M} . c) joint $d_{SLP,T2M}$ and $\theta_{SLP,T2M}$ metrics.

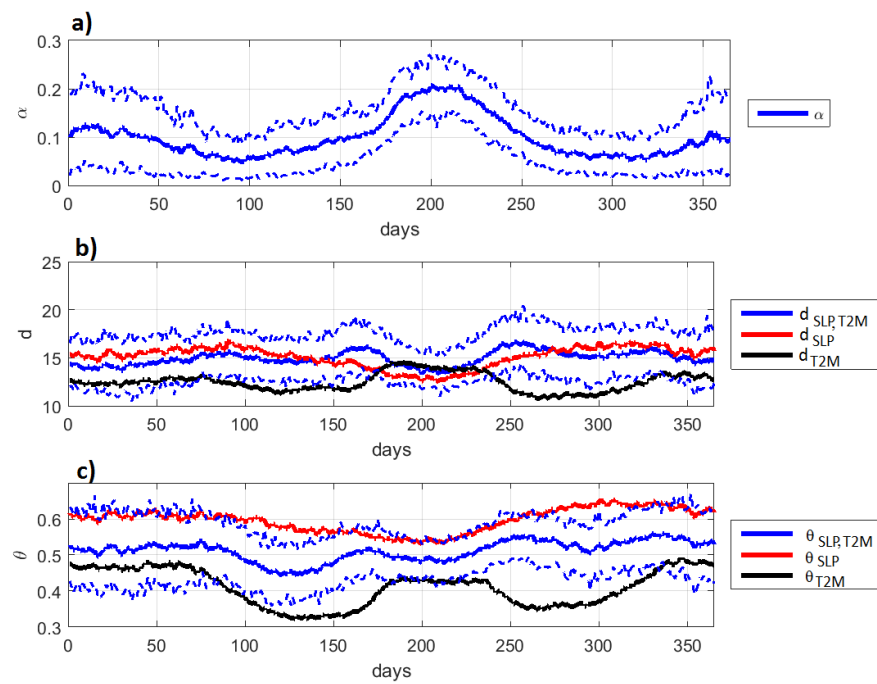


Fig. 6 Seasonal cycles of co-recurrence ratio α (a), local dimension d (b) and inverse persistence θ (c). The continuous red, black and blue lines in panels (b, c) correspond to d , θ computed on SLP, T2M and both variables jointly, respectively. The dashed lines mark one standard deviation of the quantities represented by the blue lines.

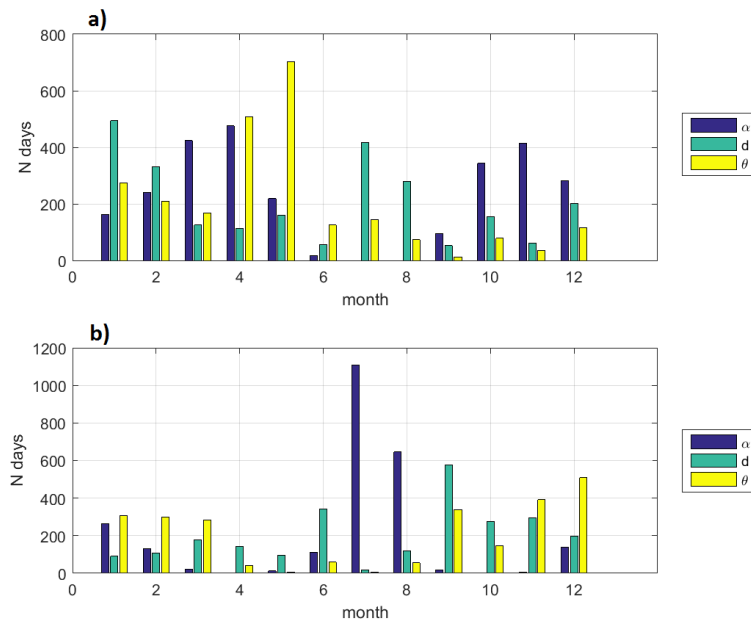


Fig. 7 Number of minima (a) and maxima (b) of co-recurrence ratio α , local co-dimension $d_{SLP,T2M}$ and local inverse co-persistence $\theta_{SLP,T2M}$ per month. These are defined as values in the lowest and highest 10 percentiles of the relevant distributions, respectively.

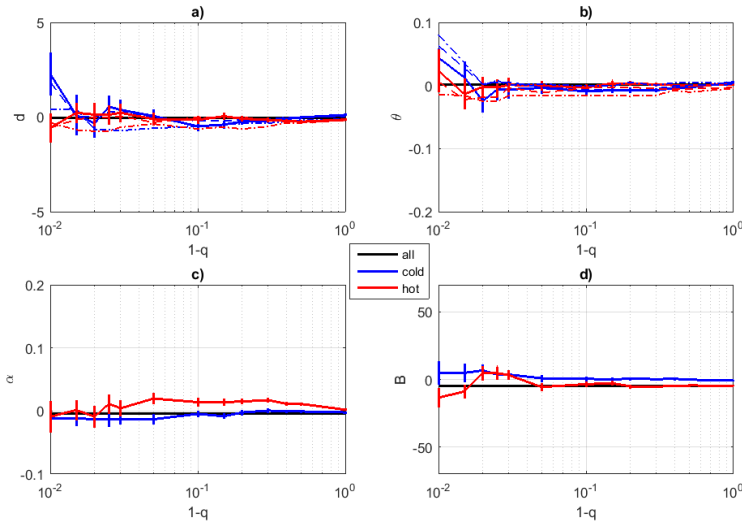


Fig. 8 Local dimensions d_{SLP} (dashed), d_{T2M} (dashed-dotted) and co-dimension $d_{SLP,T2M}$ (continuous) (a); local inverse persistences θ_{SLP} (dashed), θ_{T2M} (dashed-dotted) and inverse co-persistence $\theta_{SLP,T2M}$ (continuous) (b) and co-recurrence ratio α (c), for summer temperature extremes over Eastern North America. The values are expressed as deviations from the respective seasonal cycles. The quantiles refer to the distributions of JJA warm and cold days. The error bars indicate one standard deviation of the mean and are only shown for the continuous lines.

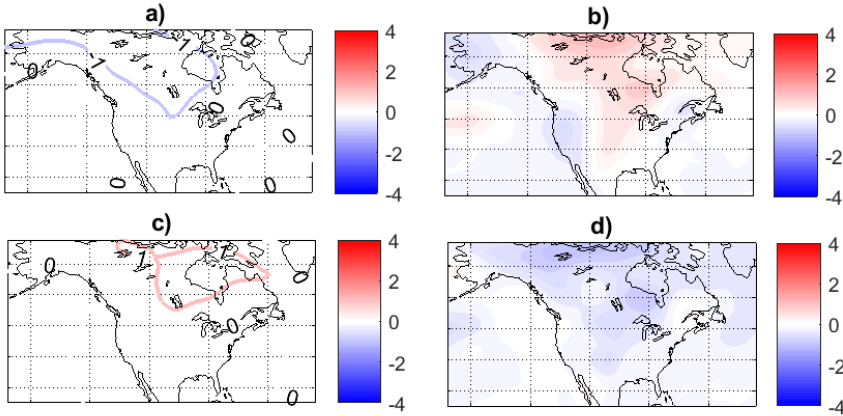


Fig. 9 Composites of sea-level pressure (SLP) anomalies in hPa (a,c) and temperature anomalies (T2M) in K (b,d) corresponding to the 10% highest (a,b) and lowest (c,d) values of deviations from the seasonal cycle of the co-recurrence ratio α during JJA. There are no regions where at least 2/3 of the composited anomalies have the same sign.

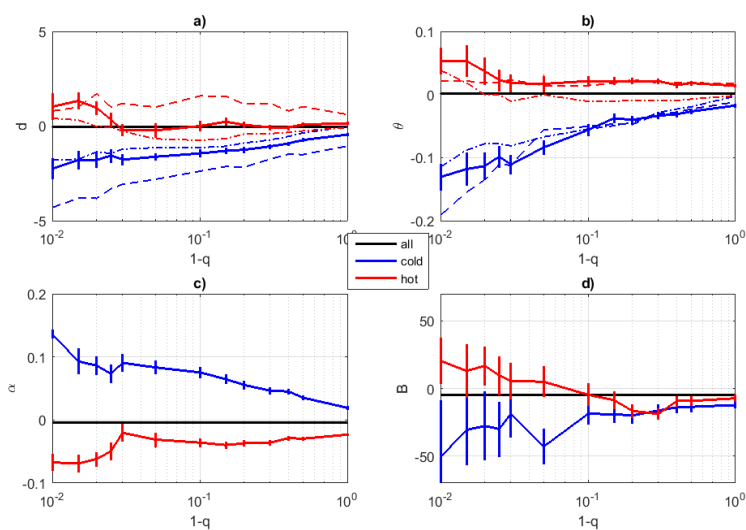


Fig. 10 Local dimensions d_{SLP} (dashed), d_{T2M} (dashed-dotted) and co-dimension $d_{SLP,T2M}$ (continuous) (a); local inverse persistences θ_{SLP} (dashed), θ_{T2M} (dashed-dotted) and inverse co-persistence $\theta_{SLP,T2M}$ (continuous) (b) and co-recurrence ratio α (c), for winter temperature extremes over Eastern North America. The values are expressed as deviations from the respective seasonal cycles. The error bars indicate one standard deviation of the mean and are only shown for the continuous lines.

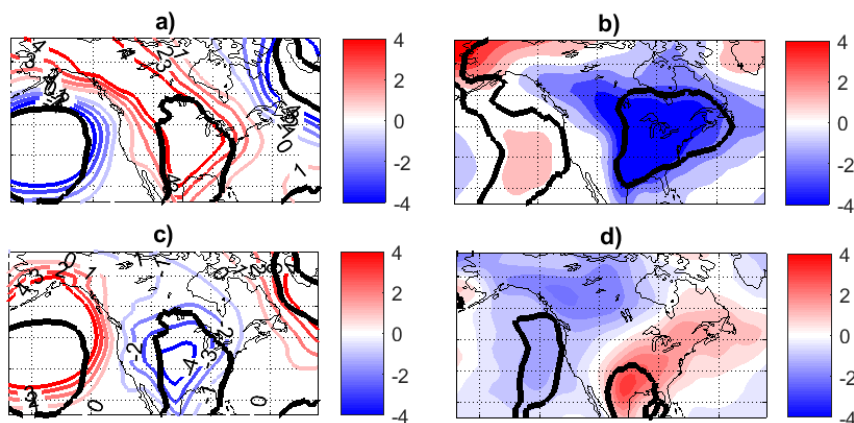


Fig. 11 Composites of sea-level pressure (SLP) anomalies in hPa (a,c) and temperature anomalies (T2M) in K (b,d) corresponding to the 10% highest (a,b) and lowest (c,d) values of deviations from the seasonal cycle of the co-recurrence ratio α , during DJF. The black lines indicate regions where at least 2/3 of the composited anomalies have the same sign.

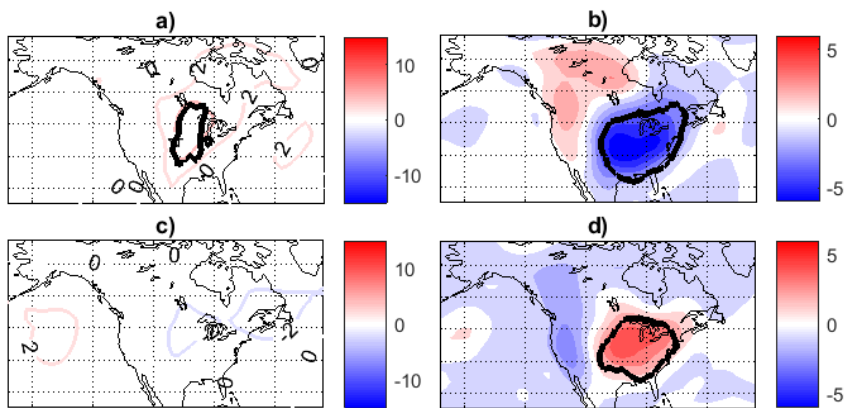


Fig. 12 Composites of sea-level pressure (SLP) anomalies in hPa (a,c) and temperature anomalies (T2M) in K (b,d) corresponding to the 10% coldest (a,b) and warmest (c,d) days during JJA. The values are expressed as deviations from the respective seasonal cycles. The black lines indicates regions where at least 2/3 of the composited anomalies have the same sign.

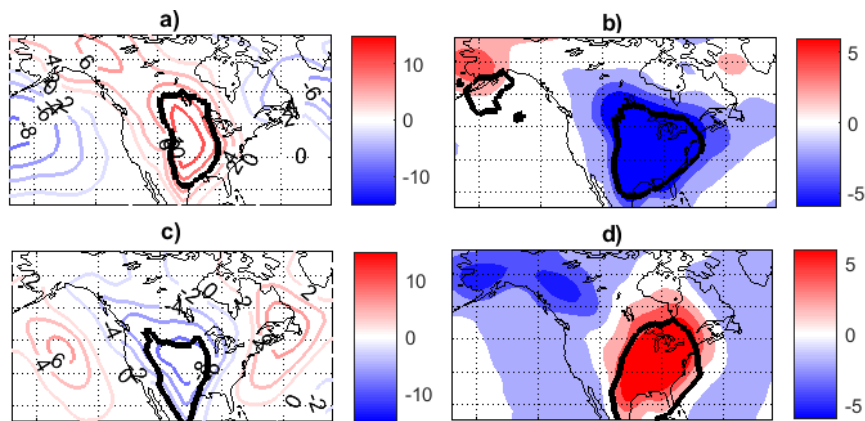


Fig. 13 Composites of sea-level pressure (SLP) anomalies in hPa (a,c) and temperature anomalies (T2M) in K (b,d) corresponding to the 10% coldest (a,b) and warmest (c,d) days during DJF. The values are expressed as deviations from the respective seasonal cycles. The black lines indicate regions where at least 2/3 of composited anomalies have the same sign.